ResearchGate

See discussions, stats, and author profiles for this publication at: https://www.researchgate.net/publication/51802362

Local Structure and Charge Distribution in Mixed Uranium–Americium Oxides: Effects of Oxygen Potential and Am Content

ARTICLE *in* INORGANIC CHEMISTRY · NOVEMBER 2011

Impact Factor: 4.76 · DOI: 10.1021/ic200910f · Source: PubMed

CITATIONS
46

READS
44

8 AUTHORS, INCLUDING:

Damien Prieur
European Commission
33 PUBLICATIONS **365** CITATIONS

SEE PROFILE

Philippe M Martin
Atomic Energy and Alternative Energies Com…
65 PUBLICATIONS **670** CITATIONS

SEE PROFILE

Andreas C Scheinost
Helmholtz-Zentrum Dresden-Rossendorf
179 PUBLICATIONS **4,386** CITATIONS

SEE PROFILE

P. Dehaudt
Atomic Energy and Alternative Energies Com…
28 PUBLICATIONS **404** CITATIONS

SEE PROFILE

Available from: Damien Prieur
Retrieved on: 31 January 2016

Inorganic Chemistry

Article

pubs.acs.org/IC

Local Structure and Charge Distribution in Mixed Uranium−Americium Oxides: Effects of Oxygen Potential and Am Content

Damien Prieur,*[,†,#] Philippe M. Martin,[‡] Aurélien Jankowiak,[§] Elisabeth Gavilan,[†] Andreas C. Scheinost,[∥] Nathalie Herlet,[†] Philippe Dehaudt,[⊥] and Philippe Blanchart[#]

[†]CEA, DEN/DTEC/SDTC/LEMA, F-30207 Bagnols-sur-Cèze Cedex, France

[‡]CEA, DEN/DEC/SESC, F-13108 Saint Paul Lez Durance Cedex, France

[§]CEA, DEN/DANS/DMN/SRMA/LC2M, F-91190 Gif-sur-Yvette, France

[∥]Helmholtz Zentrum Dresden Rossendorf (HZDR), Institute of Radiochemistry, P.O. Box 10119, 01314 Dresden, Germany

[⊥]CEA, DEN, DTEC/SDTC/DIR, F-30207 Bagnols-sur-Cèze Cedex, France

[#]GEMH, ENSCI, 87065 Limoges, France

ABSTRACT: Partitioning and transmutation (P&T) of minor actinides (MA) is currently studied to reduce the nuclear waste inventory. In this context, the fabrication of MA bearing materials is of great interest to achieve an effective recycling of these highly radioactive elements. To ensure the in-pile behavior, nuclear oxide fuels have to respect several criteria including preservation of the fluorite structure and defined oxygen to metal ratio (O/M). In the case of Am bearing materials, such as $U_{1-y}Am_yO_{2\pm x}$ (y = 0.10, 0.15, 0.20), the O/M determination is quite challenging using conventional methods (TGA, XRD) because of the particular thermodynamic properties of Am. Despite the lack of experimental data in the U−Am−O system, thermodynamical models are currently developed to effectively assess the O/M ratio. In this work, the O/M ratios were calculated for various oxygen potentials using the cation molar fraction determined by XAS measurements. These results are an important addition to the experimental data available for the U−Am−O system. Moreover, XRD and XAS indicated that the fabrication of fluorite $U_{1-y}Am_yO_{2\pm x}$ solid solution was achieved for all Am content and oxygen potentials investigated. On the basis of the molar fraction, a description of the solid solution was proposed depending on the considered sintering conditions. Finally, the occurrence of an unexpected charge compensation mechanism was pointed out.

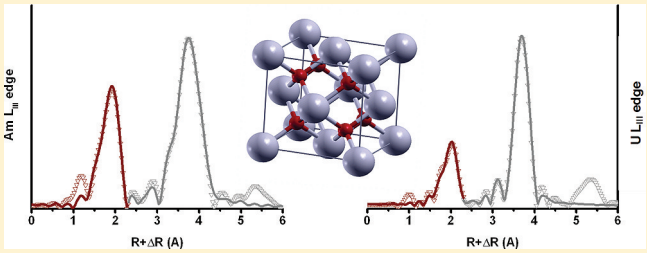

I. INTRODUCTION

Minor actinides (MA) elements, created by neutron capture in the core of pressurized water reactors (PWR), significantly contribute to the nuclear wastes radiotoxicity. In this context, partitioning and transmutation (P&T) of minor actinides (Np, Am, and Cm) is one of the main investigated strategies to significantly reduce the radiotoxic inventory.[1] Its main goal is to achieve the effective recycling of these highly radioactive elements in GEN IV Fast Neutron Reactors (FNR). The technical feasibility of MA transmutation in FNR was previously demonstrated through EFTTRA and SUPERFACT irradiation experiments.[2,3] One of the investigated P&T strategies is the heterogeneous recycling of americium in dedicated assembly elements located at the core periphery.[4,5]

In this context, $U_{1-y}Am_yO_{2\pm x}$ (y = 0.10, 0.15, 0.20) are promising blanket fuels. Before their introduction in the reactor core, fuel pellets have to meet several criteria in terms of density, geometry, composition, etc. Among them, the stoichiometry of the solid solution, commonly described as oxygen to metal atom ratio (O/M) is a very important parameter because it affects thermal, chemical, and physical properties of the fuel during irradiation and can modify the chemical reactivity of the fuel with the cladding material.

The O/M ratio parameter is fixed during the sintering step of fuel fabrication. For $U_{1-y}Am_yO_{2\pm x}$ fuels, although the fabrication of these compounds was performed at the laboratory scale, it remained challenging to achieve a targeted O/M value. In the case of $(U,Pu)O_2$ fuels, various methods are validated and used such as X-ray diffraction measurements,[6] oxygen analysis,[7] and thermogravimetric methods.[8] Furthermore, several thermodynamical models were developed for UO_2[9] and $(U,Pu)O_{2-x}$[10,11] to determine the variation of the stoichiometry as a function of both temperature and oxygen potential. The oxygen potential $\Delta\bar{G}O_2$ is generally defined by the thermodynamic relationship 1

$$\Delta\bar{G}O_2 = RT \ln\left(\frac{p_{O_2}}{p^*_{O_2}}\right) \tag{1}$$

Received: May 1, 2011

 © XXXX American Chemical Society

where R is the gas constant, T the temperature, p_{O_2} the oxygen partial pressure, and $p^*_{O_2}$ is the standard-state pressure (0.101 MPa).

For $U_{1-y}Am_yO_{2\pm x}$ (y = 0.10, 0.15, 0.20) compounds, accurate determination of the O/M ratio is not as well established as for conventional $(U,Pu)O_2$ fuels. The above-mentioned methods are currently difficult to transfer to the Am bearing materials. A limiting aspect is the high radiotoxicity of Am, which requires particular safety conditions, such as remote handling in hot cells or working with very limited quantities in glove boxes. Moreover, americium oxides exhibit very specific thermodynamic properties since they have an oxygen potential 200 kJ·mol^{-1} higher as compared to other actinides oxides. This behavior makes it difficult to monitor/obtain a targeted O/M ratio after sintering. To overcome this problem, several thermodynamical modeling approaches on $(U,Am)O_2$ and $(U,Pu,Am)O_2$ systems were proposed.[12−14] However, these are based on experimental data only available for the Am−O system[15,16] and $U_{0.50}Am_{0.50}O_{2-x}$ compounds.[17] Since one of the optimal fuel composition for MA recycling is $U_{0.85}Am_{0.15}O_{2\pm x}$, additional experimental data points of oxygen potentials−temperature−composition are needed to refine the thermochemical modeling and to adjust it to this later composition.

We propose in our study an original approach based on a coupled X-ray diffraction and X-ray absorption spectroscopy characterization of $U_{1-y}Am_yO_{2\pm x}$ (y = 0.10, 0.15, 0.20) as a function of oxygen potential. By combining these two techniques, both long-range order and short-range order have been probed in our materials. Furthermore, XAS is a suitable method to assess supplementary data since it allows obtaining atomic local environment and information on cation valence state. XAS is a powerful analytical tool for the characterization of actinide oxides.[18−25] For the specific case of americium bearing materials, XAS studies are limited to AmO_2,[26,27] $(Zr,Y,Am)O_2$,[18,19,28] $AmAlO_3$,[29] $Pb_2Se_2AmCu_3O_8$,[30] and $Am(OH)_3$.[31]

In this work, XRD and XAS experiments were conducted on five samples $U_{1-y}Am_yO_{2\pm x}$ containing variable Am contents and sintered in different atmospheres. Both electronic and atomic structures were investigated for each sample. The influence of the oxygen potential is discussed in the first part and the effect of the Am content in the second part of this paper.

II. EXPERIMENTAL SECTION

II.1. Sample Preparation. $U_{1-y}Am_yO_{2\pm x}$ with (y = 0.10, 0.15, and 0.20) compounds were fabricated by a conventional powder metallurgy process in the ATALANTE hot cells.[32,33] First, an AmO_2−UO_2 master blend was ball-milled for 30 min using stainless steel container. Then, the remaining UO_2 powder was added to adjust the composition, and a second ball milling step was carried for 30 min. Powders were uniaxialy pressed with simple effect at 400 MPa: the lower punch remains fixed during the pressing step. All pellets were sintered at 2023 K during 4 h. The different sintering atmospheres were obtained by monitoring the flow rate of both Ar−4%H_2 and Ar−O_2 gas. The studied oxygen potential ranged between −520 and −390 kJ·mol^{-1}. A dry inert atmosphere (N_2) was maintained during the materials storage period to prevent any further oxidation of the pellets at room temperature. The samples were then ground for both XRD and XAS measurements. For this later experiment, 1.2 mg of $U_{1-y}Am_yO_{2\pm x}$ powder was mixed with 15 mg of BN using a mortar and pestle. The resulting mixture was pressed and then confined in two independent sealed holders.

TIMS (thermal ionization mass spectrometer) analyses were performed on both green and sintered samples. A VG-54 magnetic sector mass spectrometer was used. An internal standard which both isotopic composition and concentration are known was added to the sample. Finally, the Am content can be determined from the measured sample final concentration and the known internal standard concentration.

II.2. XRD Data Acquisition. XRD analyses were carried using a Bruker D8 Advance diffractometer operating in Bragg−Brentano reflection geometry with a Mo($K_{\alpha 1}$) radiation especially equipped for radioactive materials measurements. An internal standard (Au) was added to the powdered samples for 2θ calibration of the XRD peak position. The FULLPROF program[34] was used for lattice parameter refinement.

II.3. XAS Data Acquisition and Analysis. XANES and EXAFS measurements were performed at the European Synchrotron Radiation Facility (ESRF, Grenoble, France), under dedicated operating conditions (6.0 GeV, 170−200 mA), on Rossendorf BeamLine (ROBL). Double crystal monochromator mounted with Si (111) crystals were used. Samples were held at 20 K using a closed-cycle helium cryostat. Data were collected in both transmission and fluorescence modes at uranium L_{III} (17166 eV), americium L_{III} (18510 eV), and uranium L_{II} (20948 eV) edges. Fluorescence signal was measured with a 13-element Ge solid state detector using a digital amplifier (XIA). Energy calibrations were achieved by using Y (17038 eV), Zr (17998 eV) and Mo (20000) Zr foils located between the second and the third ionization chamber. The E_0 values were taken at the first inflection point using the first zero-crossing value of the second derivative. The position of white line maximum was selected with the first zero-crossing of the first derivative. A minimum of two spectra were collected per edge. For each spectrum XANES spectra of the reference foil detailed before was systematically collected at the same time. The data intervals were typically 0.8 eV or 1.0 for XANES and 0.05 Å^{-1} for EXAFS. Before averaging scans, each scans were aligned using the XANES spectra collected on reference foils. The observed E_0 variations between scans were less than to 0.2 eV. As discussed by Conradson et al.,[35,36] even if the interval between points during the scans was typically 0.8 eV, the accuracy of the tabulated energies are ranging from 0.2 to 0.3 eV, especially considering that spectra were collected during the same run of experiment.

To determine oxidation states of U and Am cations, XANES spectra at L_{III} edge were compared to data collected on reference compounds on the same beamline (BM20) using the same experimental setup. For uranium, the reference compounds were $UO_{2.00}$ and $U_4O_{9-\delta}$. Their structures were confirmed using both XRD and neutron diffraction.[37] For americium, $Am^{+IV}O_2$[28] and a mixed oxalate $(U^{+IV}{}_{0.9},Am^{+III}{}_{0.1})_2(C_2O_4)_5,6H_2O$[20] were used. The cations molar fractions were assessed using a linear combination of reference compounds from the normalized μ(E) spectra. Experimental data were fitted between −20 eV and +30 eV compared to the white line position.

EXAFS spectra were collected up to 18 Å^{-1} at the Am L_{III} edge. The EXAFS spectra at the U−L_{II} edge could be collected only to 13.2 Å^{-1} (22600 eV) because of the presence of a small amount of neptunium resulting from the americium decay. The ATHENA software[38] was used for extracting EXAFS oscillations from the raw absorption spectra. Experimental EXAFS spectra were Fourier-transformed using a Kesser−Baisel window over the full k-range available at the respective edges. Curve fitting with ARTEMIS software[38] was performed in k^3 for the R range 1.0 to 5.7 Å. Phases and amplitudes for the interatomic scattering paths were calculated with the ab initio code FEFF8.40.[39]. Spherical 7.5 Å clusters of atoms build using the UO_2 fluorite type structure (space group = $Fm3\bar{m}$) were used for FEFF calculations. This symmetry can be described as a simple cubic packing of anions with cations in the cubic (8-coordinate) holes. It means that the cations are surrounded by 8 anions, 12 cations, and 24 anions. Each cation position in the cluster of atoms was filled with 50% Am and 50% U. Considering the negligible difference in calculated both amplitude and phase shift, cation−cation shells were modeled using one metal backscattered. The $S_0{}^2$ value was set at 0.90 for both U and Am shells. The shift in threshold energy (ΔE_0) was varied as a global parameter.

Table 1. Sintering Conditions, Lattice Parameters, and the First Two Coordination Shells Calculated by XRD distances of $U_{0.85}Am_{0.15}O_{2\pm x}$ Compounds

sample	sintering conditions	composition	a_0 (Å)	a_t (Å)	first shell metal−O (Å)	second shell metal−metal (Å)
A	2023 K/−520 kJ·mol^{-1}	$U_{0.85}Am_{0.15}O_{2\pm x}$	5.467 (1)	5.476(1)	2.371	3.872
B	2023 K/−450 kJ·mol^{-1}	$U_{0.85}Am_{0.15}O_{2\pm x}$	5.464(1)	5.473 (1)	2.370	3.870
C	2023 K/−390 kJ·mol^{-1}	$U_{0.85}Am_{0.15}O_{2\pm x}$	5.461 (1)	5.471 (1)	2.369	3.869
D	2023 K/−520 kJ·mol^{-1}	$U_{0.90}Am_{0.10}O_{2\pm x}$	5.469 (1)	5.475 (1)	2.371	3.871
E	2023 K/−520 kJ·mol^{-1}	$U_{0.80}Am_{0.20}O_{2\pm x}$	5.466(1)	5.476(1)	2.371	3.872

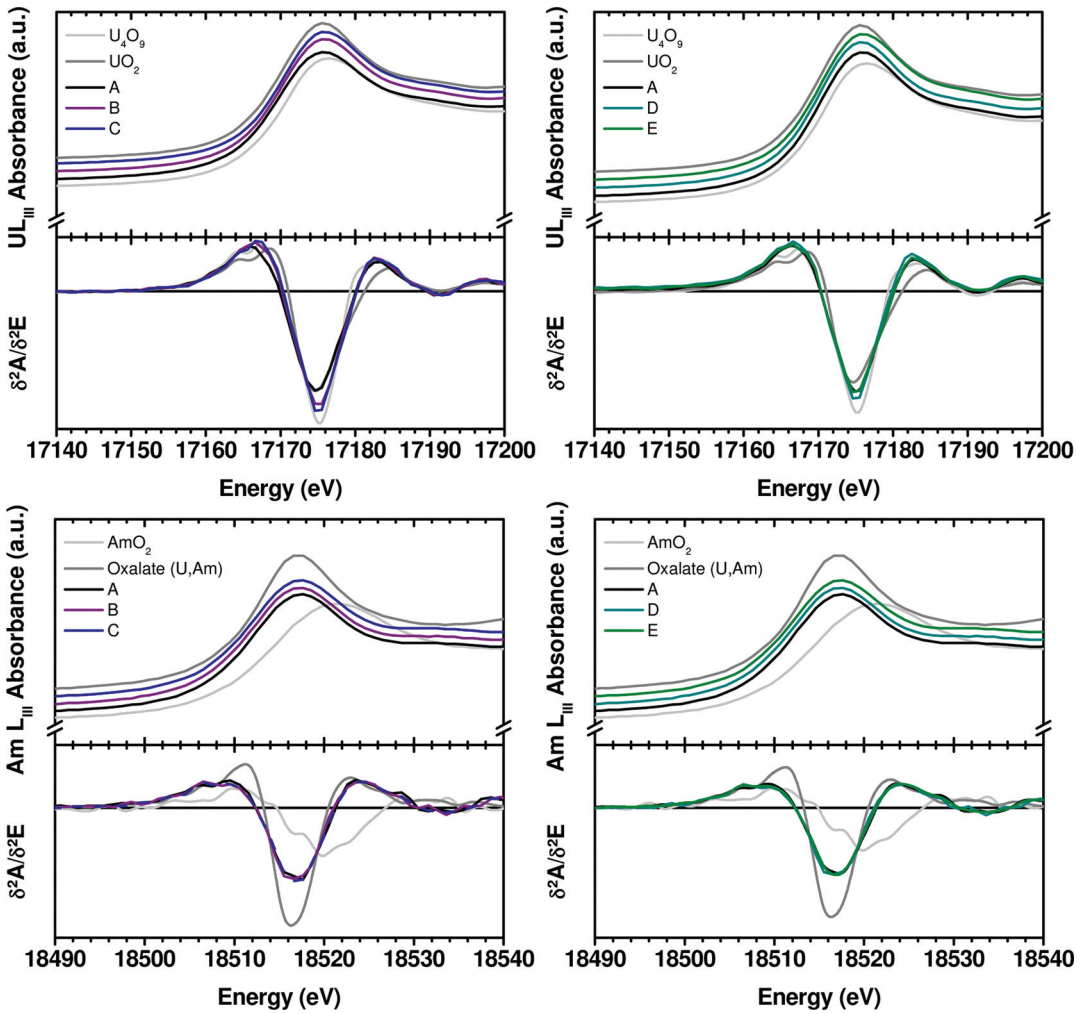

Figure 1. XANES spectra and their second-derivatives at Am L_{III} and U L_{III} edges.

III. RESULTS

III.1. XRD Measurements. The studied compounds and their corresponding sintering conditions are summarized in Table 1. The two lattice parameters a_0 and a_t measurements were respectively performed 3 days after the sample fabrication and one week before the XAS acquisition. Depending on the Am content, it corresponds to α decay doses which are ranging from 0.03 to 0.06 dpa (displacements per atom) for the a_0 value. In the case of the lattice parameter a_t, the corresponding cumulative doses are ranging from 0.20 to 0.30 dpa. The effect of oxygen potential can be observed with the three $U_{0.85}Am_{0.15}O_{2\pm x}$ samples (A, B, and C). The effect of americium content is studied with samples A, D, and E, which contain 10%, 15%, and 20% of Am. According to XRD analysis, a single-phased fluorite compounds is observed whatever sintering conditions and Am contents. The metal−oxygen and metal−metal distances given in Table 1 were calculated using the lattice parameter a_t.

III.2. XANES Results. XANES spectra collected at L_{III} edge for Am and U and the corresponding second-derivatives are compared with reference compounds in Figure 1. The energy positions of inflection points and white lines are given in Table 2. Regarding the Am L_{III} edge, there is no shift of the position of white lines and inflection peaks indicating that the oxidation state of Am is identical for all the samples. The conclusion is quite straightforward since no deviation from values obtained for Am(+III) is observed. Concerning uranium, XANES spectra show a slight shift of white line positions compared to $UO_{2.00}$ but remain systematically below the positions observed for U_4O_9 (Figure 1). Furthermore, the presence of U(+VI) can be

Table 2. Position of the Inflection Point and the White Line of the XANES Spectra Presented in Figure 1

			Am L_{III} edge		U L_{III} edge	
sample	sintering conditions	composition	inflection point (eV)	white line (eV)	inflection point (eV)	white line (eV)
A	2023 K/−520 kJ·mol^{-1}	$U_{0.85}Am_{0.15}O_{2\pm x}$	18512.5	18517.7	17169.9	17175.5
B	2023 K/−450 kJ·mol^{-1}	$U_{0.85}Am_{0.15}O_{2\pm x}$	18512.3	18517.7	17170.2	17175.6
C	2023 K/−390 kJ·mol^{-1}	$U_{0.85}Am_{0.15}O_{2\pm x}$	18512.7	18517.7	17170.3	17176.1
D	2023 K/−520 kJ·mol^{-1}	$U_{0.90}Am_{0.10}O_{2\pm x}$	18512.4	18517.7	17170.2	17175.5
E	2023 K/−520 kJ·mol^{-1}	$U_{0.80}Am_{0.20}O_{2\pm x}$	18512.3	18517.8	17170.3	17175.7
reference compound		UO_2			17169.7	17175.6
reference compound		$UO_{2.25}$			17170.8	17176.4
reference compound		$Am^{+IV}O_2$	18514.2	18521.5		
reference compound		$(U^{+IV}{}_{0.9}, Am^{+III}{}_{0.1})_2(C_2O_4)_5, 6H_2O$	18512.4	18517.7		

excluded, because the shoulder located at ∼15 eV after the main peak associated with uranyl type unit and observed for U_3O_8 and higher uranium oxide[36] is not present in our spectra.

Since U_4O_9 is the most hyperstoichiometric uranium oxide (O/M = 2.25) exhibiting a cubic structure at room temperature, it was chosen as a reference compound in our study because no deviation from cubic symmetry was observed by XRD in our samples. Assuming that the latter is a mixture of 50% U(+IV) and 50% U(+V), it can be concluded that there is a U(+IV)/U(+V) mixed valence. Note that the presence of U(V) in $U_{0.50}Am_{0.50}O_{2\pm x}$ was discussed by Mayer et al.[40] based on XPS measurements.

As mentioned in the Experimental Section, U(+IV) and U(+V) molar fractions were determined by fitting experimental data using a linear combination of UO_2 and U_4O_9. As illustrated in Figure 2 with results obtained for sample B (R factor = 3×10^{-4}, χ^2 = 0.02), a very good agreement between experimental and fitted data were obtained. For all the samples, the R factor and the χ^2 are respectively inferior or equal to 4×10^{-4} and 0.03 as shown in Table 3. This supports the validity of both calculated cation molar fractions and O/M ratios given in Table 3. These results will be commented in the discussion part. However, it is important to mention that the molar fractions of Am(+III), U(+IV), and U(+V) are very important additional experimental data of oxygen potential−temperature−composition, performed at high temperature, and are an important addition to the very few available experimental data. We are currently using these new data to refine our thermodynamic modeling[12] in order to define the optimum sintering conditions for $U_{1-y}Am_yO_{2\pm x}$ and to predict the associated O/M ratio for these sintering conditions.

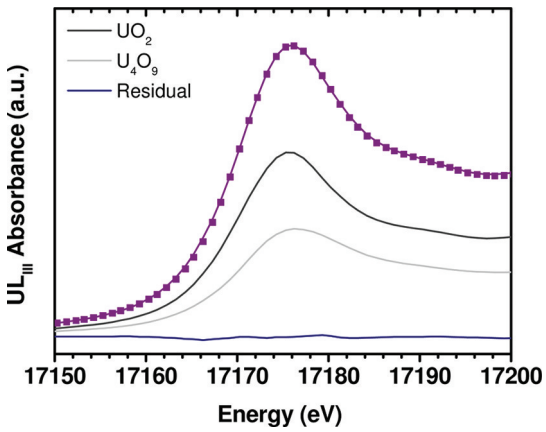

Figure 2. Fit of XANES spectra collected on sample **B**.

Table 3. Molar Fraction of Am(+III), Am(+IV), U(+IV), and U(+V)

	molar fraction (%)				fit of XANES		
sample	Am(+III)	Am(+IV)	U(+IV)	U(+V)	R factor	χ^2	O/M
A	15	0	71	14	3×10^{-4}	0.03	2.00
B	15	0	70	15	4×10^{-4}	0.03	2.00
C	15	0	62	23	3×10^{-4}	0.02	2.04
D	10	0	81	9	3×10^{-4}	0.02	2.00
E	20	0	63	17	4×10^{-4}	0.03	1.99

III.3. EXAFS Results. Am L_{III} and U L_{II} experimental and fitted EXAFS spectra and their Fourier Transforms (FT) are presented in Figure 3 and Figure 4. For both cations, two intense peaks are observed in the FT as expected for the cubic face centered structure revealed with XRD. The first peak at ∼1.8 Å is because of oxygen atoms which surrounds the Am or U atoms. The second peak at ∼3.8 Å corresponds mostly to the second coordination shell of metal atoms surrounding the Am or U atoms. Regarding the samples A, D, and E, a decrease of the spectral amplitude can be observed at both edges with increasing Am content, suggesting increasing disorder. No such behavior is observed in the case of the variation of the oxygen potential.

Regarding to the Am local environment, neither additional Am−Am distances nor Am_2O_3 type distances were necessary to reproduce the experimental signal. In the case of the U L_{II} edge, a fitting model using three distinct U−O coordination shells (2.24, 2.38, and 2.55 Å) was also tested. This model is based on the U local environment in hyperstoichiometric UO_{2+x} ($0 \leq x \leq 0.24$) materials presented by Conradson et al.[36] This fit did not reproduce the experimental data any better than the one obtained with the simple fluorite model. Furthermore, no uranyl type U−O distance (∼1.8 Å) could be confirmed. It is important to mention that a neutron diffraction study performed by Garrido et al.[41] contradicts the EXAFS conclusions of Conradson et al.[36] Therefore, the crystallographic distances, at the U L_{II} edge, were also calculated using a fluorite model.

Fitting results are shown in Figure 3 and Figure 4 and associated metric values are given in Table 4. As demonstrated by both the very low R-factor and the good agreement between experimental and fitted spectra, the fluorite solid solution is systematically obtained. This is also supported by XRD measurements. At the Am L_{III} edge, the bond length of the first oxygen atoms surrounding Am is about 2.42 Å, which is significantly longer than the 2.37 Å of UO_2 (cf. Table 1). This elongation can be attributed to the larger ionic radius of Am(+III) ($r(Am^{3+})$ = 1.09 Å; $r(Am^{4+})$ = 0.95 Å, $r(U^{4+})$ = 1.00 Å,

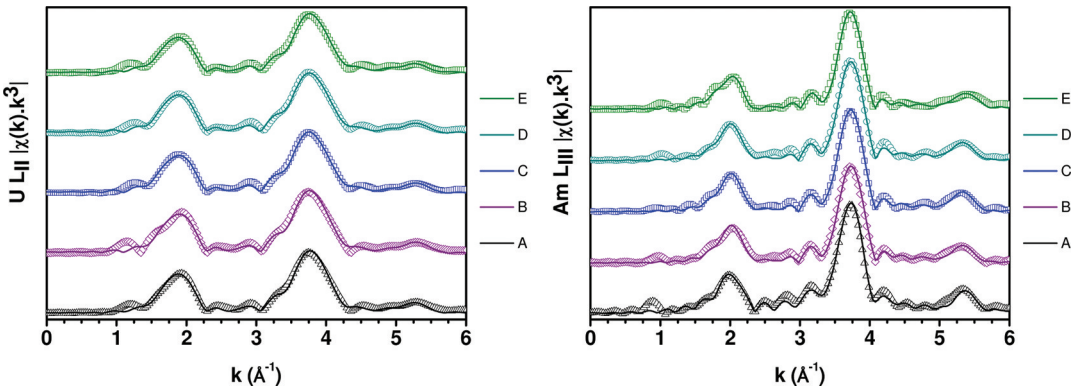

Figure 3. Fourier transforms of experimental and fitted EXAFS spectra collected at Am L_{III} and U L_{II} edges (○ : data; — : fit).

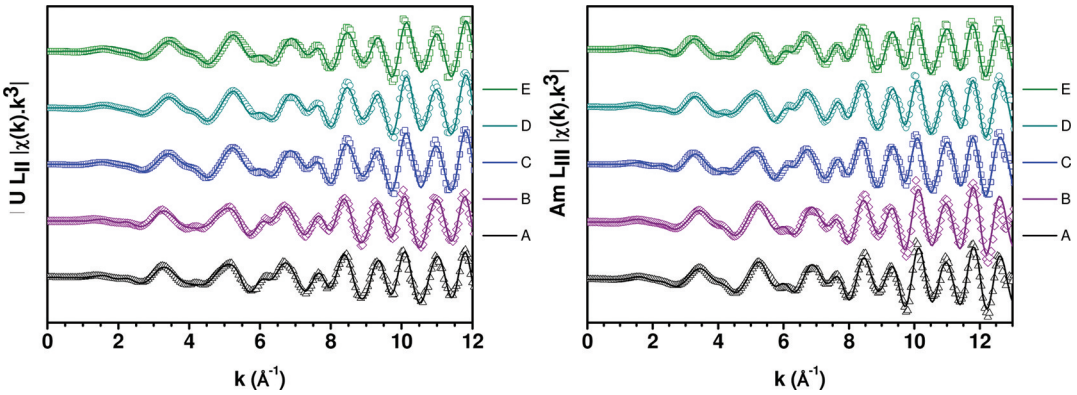

Figure 4. Experimental and fitted EXAFS spectra at Am L_{III} and U L_{II} edges (○ : data; — : fit).

$r(U^{5+})$ = 0.89 Å[42]). For the studied samples, the coordination value of the metal−metal shell is equal to the crystallographic value of 12.0(5). Both Am−U and Am−Am distances are approximately equal to 3.86 Å which is lower than those calculated from the XRD measurements. The Am−O third shell distance slightly decreases while both oxygen potential and Am content increasing. Regarding to the U L_{II} edge, the bond length of the first oxygen atoms surrounding the U is about 2.35 Å. The U−U distances of 3.87 Å, are in agreement with values obtained from the XRD measurement. Therefore, all of our data confirm the simple fluorite structure. Changing the *k*-weighting to k^1, k^2, or k^3 does not significantly change the results. Moreover, the increase of the Am−O distance and the decrease of the U−O distance are consistent with a solid solution, which is composed of U(+IV), U(+V), and Am(+III).

The Table 4 also shows that coordination values of the first and the third cation-oxygen shell are respectively equal to 8.0(5) and 24.0(5). These results point out the absence of oxygen vacancies randomly distributed in the lattice and are therefore in agreement with the O/M close to 2.00 (Table 3). Comparing to $(U,Ln)O_{2-x}$, the stoichiometry of $(U,Am)O_{2\pm x}$ solid solution is unexpected for these sintering conditions. Indeed, $(U_{0.7}Nd_{0.3})O_{2-x}$ has an O/M ratio of 1.96 at 1300 °C for an oxygen potential equal to −400 kJ·mol^{-1} while a $(U_{0.8}La_{0.2})O_{1.97}$ solid solution is obtained at 1273 K and −460 kJ·mol^{-1}. However, both XANES and EXAFS data strongly supports the stoichiometry of the uranium and americium mixed oxides solid solution. Mechanisms explaining the stoichiometric solid solution formation will be proposed in the discussion part.

IV. DISCUSSION

IV.1. Effect of Oxygen Potential. A previous study[12] has shown that the sintering behavior of the $U_{1-y}Am_yO_{2\pm x}$ compounds is strongly affected by the oxygen potential. Indeed, americium based oxides exhibit high oxygen potentials compared to other actinides oxides, such as UO_2.[9] One of the main associated risks is an excessive reduction of Am oxides leading to sublimation of metallic americium and/or Am gaseous species formation. These phenomena can occur even at relatively low temperature (above 1200 K).

Regarding to the above-mentioned results on samples A, B, and C and especially the XANES measurements detailed in Figure 1, Am is in the trivalent state while a mixed valence of U(+IV)/U(+V) is present whatever the oxygen potential value. A complete reduction of Am(+IV) to Am(+III) during the sintering process is thus observed. P. Martin et al.[43] have already observed that Am(+IV) is easily reduced to Am(+III). In our case, TIMS analyses indicate that no volatilization of Am occurred during the sintering.

According to the UO_{2+x} oxygen potential curves given in Figure 5,[9] a fully reduced solid solution $U_{1-y}Am_yO_{2-y/2}$ with a high concentration of oxygen vacancies in the anion sublattice as well as U(+IV) and Am(+III) ions distributed in the cation sublattice would be expected for sintering in Ar−H_2 atmosphere. In contrast, our work shows, as illustrated by Table 4, that no oxygen vacancy randomly distributed in the lattice are present and that both Am(+III) and U(+V) can coexist with identical molar fractions at the lowest oxygen potentials, that is, −520 and −450 kJ·mol^{-1}. These results were not expected since the U(+V) cation existence is not predicted by the UO_{2+x} oxygen potential curves. Indeed, according to

Table 4. Crystallographic Distances Extracted by Fitting of EXAFS Spectra Measured at Both U L_{II} and Am L_{III} Edges (O* = Multiple Scattering)

sample	edge	shell	R (Å)	N	σ^2 (A^2)	R factor
A/$U_{0.85}Am_{0.15}O_{2\pm x}$ 2023 K/−520 kJ·mol^{-1}	Am	O	2.427(5)	7.9(5)	0.004(1)	0.015
		Am and U	3.861(5)	11.5(5)	0.003(1)	
		O	4.51(1)	24.0(5)	0.011(1)	
		O*	4.91(1)	7.9(5)	0.004(1)	
		Am and U	5.48(2)	6(1)	0.003(1)	
	U	O	2.342(5)	7.9(5)	0.006(1)	0.016
		Am and U	3.870(5)	11.6(5)	0.003(1)	
		O	4.47(1)	24.1(5)	0.012(1)	
		O*	4.66(1)	7.9(5)	0.006(1)	
		Am and U	5.45(2)	6(1)	0.004(1)	
B/$U_{0.85}Am_{0.15}O_{2\pm x}$ 2023 K/−450 kJ·mol^{-1}	Am	O	2.431(5)	7.7(5)	0.006(1)	0.014
		Am and U	3.862(5)	11.7(5)	0.005(1)	
		O	4.51(1)	24.3(5)	0.012(1)	
		O*	4.93(1)	7.7(5)	0.006(1)	
		Am and U	5.47(2)	6(1)	0.007(1)	
	U	O	2.343(5)	8.1(5)	0.006(1)	0.016
		Am and U	3.870(5)	11.8(5)	0.004(1)	
		O	4.46(1)	24.0(5)	0.010(1)	
		O*	4.67(1)	8.1(5)	0.006(1)	
		Am and U	5.45(2)	6(1)	0.005(1)	
C/$U_{0.85}Am_{0.15}O_{2\pm x}$ 2023 K/−390 kJ·mol^{-1}	Am	O	2.437(5)	7.7(5)	0.007(1)	0.01
		Am and U	3.865(5)	11.7(5)	0.005(1)	
		O	4.51(1)	24.0(5)	0.013(1)	
		O*	4.94(1)	7.7(5)	0.007(1)	
		Am and U	5.47(2)	6(1)	0.007(1)	
	U	O	2.346(5)	8.4(5)	0.007(1)	0.014
		Am and U	3.871(5)	11.8(5)	0.004(1)	
		O	4.47(1)	23.8(5)	0.012(1)	
		O*	4.67(1)	8.4(5)	0.007(1)	
		Am and U	5.45(2)	6(1)	0.004(1)	
D/$U_{0.90}Am_{0.10}O_{2\pm x}$ 2023 K/−520 kJ·mol^{-1}	Am	O	2.428(5)	7.8(5)	0.005(1)	0.014
		Am and U	3.861(5)	11.7(5)	0.003(1)	
		O	4.51(1)	24.0(5)	0.003 (1)	
		O*	4.92(1)	7.8(5)	0.005(1)	
		Am and U	5.48(2)	6(1)	0.003(1)	
	U	O	2.338(5)	8.1(5)	0.006(1)	0.015
		Am and U	3.867 (5)	11.8(5)	0.003 (1)	
		O	4.47 (1)	23.8(5)	0.012 (1)	
		O*	4.65 (1)	8.4(5)	0.006 (1)	
		Am and U	5.45 (2)	6(1)	0.004 (1)	
E/$U_{0.80}Am_{0.10}O_{2\pm x}$ 2023 K/−520 kJ.mol^{-1}	Am	O	2.434(5)	7.9(5)	0.006(1)	0.015
		Am and U	3.864(5)	11.6(5)	0.003(1)	
		O	4.49(1)	24.0(5)	0.009(1)	
		O*	4.93(1)	7.9(5)	0.006(1)	
		Am and U	5.48(2)	6(1)	0.004(1)	
	U	O	2.339(5)	7.9(5)	0.007(1)	0.016
		Am and U	3.867(5)	11.9(5)	0.003(1)	
		O	4.47(1)	24.0(5)	0.012(1)	
		O*	4.65(1)	7.9(5)	0.005(1)	
		Am and U	5.46(2)	6(1)	0.004(1)	

Figure 5, U should be tetravalent at these sintering conditions. Both partial oxidation of U(+IV) to U(+V) and oxygen vacancies absence might be explained by one of the two following mechanism. First, considering that the self-diffusion occurs between Am(+IV) and U(+IV), the presence of U(+V) can be understood from an electronic charge transfer between U(+IV) and Am(+IV). Such a mechanism has already been observed using electrical conductivity measurements in $U_{1-y}Pu_yO_{2\pm x}$ solid solution where a charge transfer reaction $U^{4+} + Pu^{4+} = U^{5+} + Pu^{3+}$ was suggested.[44] In other words, Am can act as an electron acceptor while U is an electron donor. Secondly, given the high oxygen potential of Am[16,45] (Figure 5), it can be also supposed that the reduction of Am(+IV) to Am(+III) occurs before the solid solution formation. In comparison with the lanthanides doped UO_2, the substitution of a tetravalent U by a trivalent cation leads to the partial

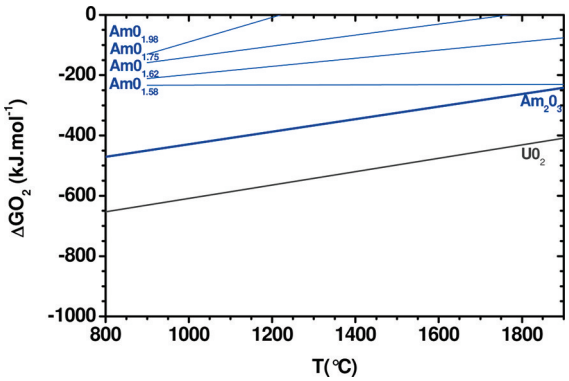

Figure 5. Oxygen potential of AmO_{2-x} and UO_2 as a function of the temperature.

oxidation of U(+IV) to U(+V) (or U(+VI)) by a charge compensation mechanism to maintain the structure electroneutrality.[46−48] In this case, the substitution of U(+IV) by Am(+III) leads to the partial oxidation of U and the solid solution formation. Both of these above-mentioned mechanism explain the oxygen vacancies absence and the presence of U(+V) and Am(+III) in the same proportion. For the oxygen potentials ranging from −520 to −450 kJ.mol^{-1}, the solid solution can be described by $U^{4+}_{1-2y}U^{5+}_{y}Am^{3+}_{y}O_2$. Additional TGA and high temperature XRD are required to confirm one of the discussed mechanism.

Moreover, as presented in Figure 6, the U(+V) molar fraction is significantly higher than that of Am(+III) for an

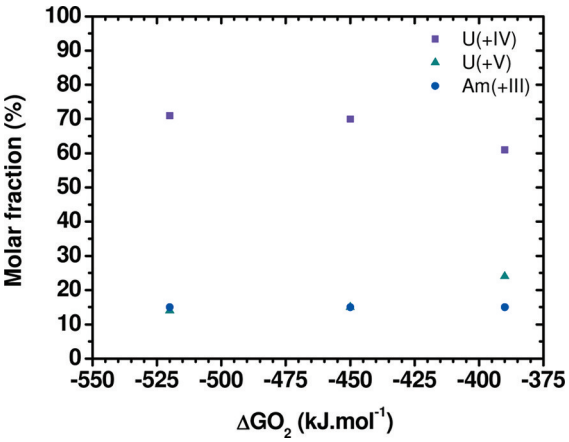

Figure 6. Molar fractions of U(+IV), U(+V), and Am(+III) as a function of the oxygen potential.

oxygen potential equal to −390 kJ·mol^{-1}. It can be understood from the increase of the oxygen partial pressure which leads to oxygen atoms insertion in the structure conducting to the partial oxidation of U(+IV) to U(+V). Thus, for very low oxygen potentials, the U(+V) formation is due to the above-mentioned mechanism while, for higher oxygen partial pressure, there is also an additional contribution which corresponds to the oxygen atom insertion into interstitial positions.

It is important to mention that the molar fractions of Am(+III), U(+IV), and U(+V), given in Table 3, are very important additional experimental data of oxygen potential-temperature-composition, performed at high temperature, and are an important contribution to the very few available experimental data. We are currently using these new data to refine our thermodynamic modeling[12] to define the optimum sintering conditions for $U_{1-y}Am_yO_{2\pm x}$ and to predict the O/M ratio for these sintering conditions.

The XAFS results show that the oxygen potential mainly affects the crystallographic distances and the coordination number. As presented in Table 4, both third-shell Am−O and U−O distances decrease with increasing oxygen partial pressure. It can be concluded that the insertion of additional oxygen atoms in the lattice results in a reduction of the longest distances. This conclusion is in good agreement with the increase of Debye−Waller factor indicating that the disorder of the local structure increases with oxygen potential.

IV.2. Effect of Americium Content. Samples D, A, and E containing respectively 10, 15 and 20% of Am were sintered under the same sintering conditions (2023 K, −520 kJ·mol^{-1}). According to the XAFS spectra presented in Figure 4, solid solutions were obtained for all the samples. As expected in the case of a solid solution, the $U_{1-y}Am_yO_{2\pm x}$ lattice parameter a_0, given in the Table 1, linearly decreases with the Am content. The lattice parameter a_0 can be described as a function of the Am content y according to the eq 2:

$$a_{0_{U_{1-y}Am_yO_{2-x}}} = a_{UO_2} - 0.0022y \quad R^2 = 0.97 \tag{2}$$

where the lattice parameter a_{UO_2} is equal to 0.54706 nm.[49]

Note that the validity of eq 2 is strictly limited to $U_{1-y}Am_yO_{2-x}$ compounds sintered under reducing conditions at 2023 K. Since several types of phases with various crystallographic symmetries might be involved in the solid solution formation, the lattice parameter can not be easily assessed with the Vegard's law. For this reason, the lattice parameter was not calculated using the Vegard's law in this paper. Moreover, the approach of Kato et al.[50] was also considered but significant differences were obtained in term of determined lattice parameter and O/M ratio. These differences with the mentioned model could be explained by a nonvegardian behavior of the $U_{1-y}Am_yO_{2-x}$ solid solution. This kind of behavior has already been pointed out in fluorite-based MO_2−$LnO_{1.5}$.[51]

Since U(+V) has a small ionic radius compared to U(+IV) and Am(+III), the lattice parameter decrease with the Am content increase is in good agreement with the presence of U(+V) in the fluorite solid solution.

Figure 7 and Table 3 show that both U(+V) and Am(+III) molar fractions are nearly equal whatever the Am content.

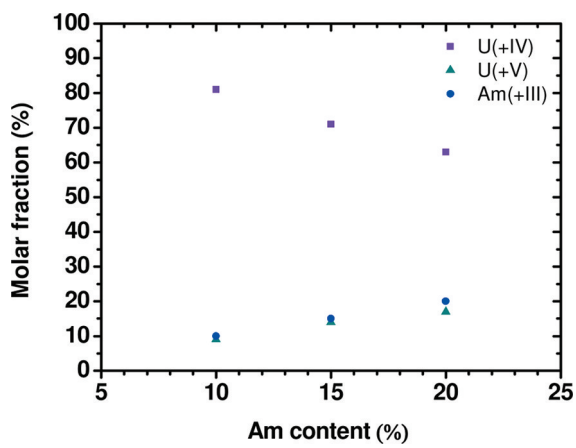

Figure 7. Molar fraction of U(+IV), U(+V), and Am(+III) as a function of the Am content.

This feature reinforces the proposed charge compensation mechanism occurring for low oxygen potentials.

The U(+V) molar fraction y' can be expressed as a function of the Am content y by the following linear regression eq 3:

$$y' = 0.91y \quad R^2 = 0.96 \tag{3}$$

As a result, for these particular sintering conditions and Am contents, the solid solution can be described as $U^{4+}_{1-1.91y}U^{5+}_{0.91y}Am^{3+}_{y}O_2$.

Regarding to the EXAFS results, there is no significant influence of the Am content on both crystallographic distances and coordination numbers. An increase of the Debye−Waller factor is, however, observed indicating a more disordered structure in the case of higher Am content. It might be explained by the presence of cations with different ionic radii, that is, Am(+III), U(+IV) and U(+V) and especially by the U(+IV)/U(+V) ratio decrease.

The increase of the disorder with the Am content can also be understood from the high α activity of Am which leads to the emission of ^{237}Np recoil nuclei inducing disorder in the structure and defect formation. Moreover, since the Np ion exist as Np(+IV), its presence has to induce a local charge transfer, enhancing probably the defect formation due to α decay.

Besides, the high α activity of ^{241}Am may also cause a significant self-irradiation inducing structural defects formation[52−54] and lattice parameter expansion.[29,55,56] Swelling phenomenon due to the high activity has already been observed at the macroscopic scale in $U_{1-y}Am_yO_{2\pm x}$ (y = 0.10, 0.20) materials.[57,58] In this present work, Table 1 points out that the lattice parameters have increased of about 0.2% during one year, which corresponds to time between the sample fabrication and the XAS experiment. This evolution, which can notably be understood from the formation of ^{237}Np recoil nuclei, can explain one part of the macroscopic swelling. Moreover, the concentration of self-irradiation induced defects, such as vacancy, is expected to be important since the cumulative α dose of the sample is about 0.20 dpa. However, the fitted coordination numbers do not confirm this assumption. This mismatch between the surrounding atoms and the defect content might be explained by the presence of defects with large open volume. Such defects were pointed out in a previous study on $U_{0.90}Am_{0.10}O_{2-x}$ compounds using positron annihilation lifetime spectroscopy.[57] It was shown that a high concentration of He stabilized vacancies could create a necessary condition for void growth and swelling. Further TEM experiments would be useful to clear this point.

V. CONCLUSION

In this work, XAS experiments were conducted with $U_{1-y}Am_yO_{2\pm x}$ compounds containing various Am contents and sintered under different atmospheres. The XANES measurements indicate that the Am(+IV) is totally reduced to Am(+III) while there is a partial oxidation of U(+IV) to U(+V). From these results, additional experimental data of oxygen potential-composition−temperature were determined and are now available to refine the thermodynamical models. It was also shown that fluorite solid solutions are obtained whatever Am content and oxygen potential. In the case of the compound sintered at −520 kJ·mol^{-1}, a description of the solid solution was proposed and it was pointed out that there is a charge compensation mechanism during the sintering. Further dilatometric and thermogravimetric tests are necessary to understand the kinetic of these phenomena.

AUTHOR INFORMATION

Corresponding Author

*E-mail: damien.prieur@neuf.fr. Tel: +3346796119.

ACKNOWLEDGMENTS

The authors thank N. Astier, M. Bataille, P. Coste for the sample preparation and their support at the European Synchrotron Radiation Facility during the XAS measurements. The authors are also grateful to B. Arab-Chapelet and R. Belin for respectively providing the XAFS spectra of AmO_2 and oxalate reference compounds. The authors acknowledge S. Petit for the gamma measurements. The authors are grateful to the European Synchrotron Radiation Facility for provision of synchrotron radiation facilities.

REFERENCES

(1) Warin, D. *J. Nucl. Sci. Technol.* **2007**, *44*, 410−414.
(2) Babelot, J.-F.; Conrad, R.; Konings, R. J. M.; Mühling, G.; Salvatores, M.; Vambenepe, G. *J. Alloys Compd.* **1998**, *271−273*, 606−609.
(3) Ogawa, T. *Prog. Nucl. Energy* **2002**, *40*, 539−546.
(4) Grouiller, J.-P.; Pillon, S.; de Saint Jean, C.; Varaine, F.; Leyval, L.; Vambenepe, G.; Carlier, B. *J. Nucl. Mater.* **2003**, *320*, 163−169.
(5) Delpech, M.; Grouiller, J. P. *NT DER/SPRC/LEDC 96−462* 1997.
(6) Schmitz, F.; Dean, G.; Halachmy, M. *J. Nucl. Mater.* **1971**, *40*, 325−333.
(7) Waterbury, G.; Metz, C. *Anal. Chem.* **1959**, *31*, 1144−1148.
(8) McNeilly, C. E.; Chikalla, T. D. *J. Nucl. Mater.* **1971**, *39*, 77−83.
(9) Lindemer, T. B.; Besmann, T. M. *J. Nucl. Mater.* **1985**, *130*, 473−488.
(10) Besmann, T. M.; Lindemer, T. B. *J. Nucl. Mater.* **1985**, *130*, 489−504.
(11) Besmann, T. M.; Lindemer, T. B. *J. Nucl. Mater.* **1986**, *137*, 292−293.
(12) Prieur, D.; Jankowiak, A.; Lechelle, J.; Herlet, N.; Dehaudt, P.; Blanchart, P. *J. Nucl. Mater.* **2011**.
(13) Osaka, M.; Namekawa, T.; Kurosaki, K.; Yamanaka, S. *J. Nucl. Mater.* **2005**, *344*, 230−234.
(14) Osaka, M.; Kurosaki, K.; Yamanaka, S. *J. Alloys Compd.* **2007**, *428*, 355−361.
(15) Chikalla, T. D.; Eyring, L. *J. Inorg. Nucl. Chem.* **1967**, *29*, 2281−2293.
(16) Casalta, S. Matzke, H.; Prunier, C. *GLOBAL 95* 1995.
(17) Bartscher, W.; Sari, C. *J. Nucl. Mater.* **1983**, *118*, 220−223.
(18) Walter, M.; Nästren, C.; Somers, J.; Jardin, R.; Denecke, M. A.; Brendebach, B. *J. Solid State Chem.* **2007**, *180*, 3130−3135.
(19) Martin, P. M.; Belin, R. C.; Valenza, P. J.; Scheinost, A. C. *J. Nucl. Mater.* **2009**, *385*, 126−130.
(20) Grandjean, S.; Arab-Chapelet, B.; Robisson, A. C.; Abraham, F.; Martin, P.; Dancausse, J.-P.; Herlet, N.; Léorier, C. *Nucl. Mater.* **2009**, *385*, 204−207.
(21) Denecke, M. A. *Coord. Chem. Rev.* **2006**, *250*, 730−754.
(22) Denecke, M. A.; Dardenne, K.; Marquardt, C. M. *Talanta* **2005**, *65*, 1008−1014.
(23) Walter, M.; Somers, J.; Bouëxière, D.; Gaczynski, P.; Brendebach, B. *J. Solid State Chem.* **2009**, *182*, 3305−3311.
(24) Martin, P.; Grandjean, S.; Valot, C.; Carlot, G.; Ripert, M.; Blanc, P.; Hennig, C. *J. Alloys Compd.* **2007**, *444−445*, 410−414.
(25) Walter, M.; Somers, J.; Bouëxière, D.; Rothe, J. *J. Solid State Chem.* **2011**, *184*, 911−914.
(26) Nishi, T.; Nakada, M.; Itoh, A.; Suzuki, C.; Hirata, M.; Akabori, M. *J. Nucl. Mater.* **2008**, *374*, 339−343.

(27) Nishi, T.; Nakada, M.; Suzuki, C.; Shibata, H.; Itoh, A.; Akabori, M.; Hirata, M. *J. Nucl. Mater.* **2010**, *401*, 138−142.
(28) Belin, R. C.; Martin, P. M.; Valenza, P. J.; Scheinost, A. C. *Inorg. Chem.* **2009**, *48*, 5376−5381.
(29) Walter, M.; Somers, J.; Fernandez, A.; Haas, D.; Dardenne, K.; Denecke, M. A. *J. Nucl. Mater.* **2007**, *362*, 343−349.
(30) Soderholm, L.; Williams, C.; Skanthakumar, S.; Antonio, M. R.; Conradson, S. *Z. Phys. B* **1996**, *101*, 539−545.
(31) Meyer, D.; Fouchard, S.; Simoni, E.; DenAuwer, C. *Radiochim. Acta* **2002**, *90*, 253−258.
(32) Prieur, D.; Jankowiak, A.; Leorier, C.; Herlet, N.; Donnet, L.; Dehaudt, P.; Maillard, C.; Laval, J.-P.; Blanchart, P. *Powder Technol.* **2011**, *208*, 553−557.
(33) Prieur, D. J.; Thibaud, A.; Nathalie, D.; H. Philippe, D.; Philippe, B. *J. Nucl. Mater.* **2011**, *414*, 503−507.
(34) Carjaval, J. R. *Satellite Meeting on Powder Diffraction of the XV IUCr Congress* 1990.
(35) Conradson, S. D.; Abney, K. D.; Begg, B. D.; Brady, E. D.; Clark, D. L.; den Auwer, C.; Ding, M.; Dorhout, P. K.; Espinosa-Faller, F. J.; Gordon, P. L.; Haire, R. G.; Hess, N. J.; Hess, R. F.; Keogh, D. W.; Lander, G. H.; Lupinetti, A. J.; Morales, L. A.; Neu, M. P.; Palmer, P. D.; Paviet-Hartmann, P.; Reilly, S. D.; Runde, W. H.; Tait, C. D.; Veirs, D. K.; Wastin, F. *Inorg. Chem.* **2004**, *43*, 116−131.
(36) Conradson, S. D.; Manara, D.; Wastin, F.; Clark, D. L.; Lander, G. H.; Morales, L. A.; Rebizant, J.; Rondinella, V. V. *Inorg. Chem.* **2004**, *43*, 6922−6935.
(37) Desgranges, L.; Baldinozzi, G.; Rousseau, G.; Niepce, J.; Calvarin, G. *Inorg. Chem.* **2009**, *48*, 7585−7592.
(38) Ravel, B.; Newville, M. *J. Synch. Rad.* **2005**, *12*, 537−541.
(39) Rehr, J. J.; Ankudinov, A.; Zabinsky, S. I. *Catal. Today* **1998**, *39*, 263−269.
(40) Mayer, K.; Kanellakopoulos, B.; Naegele, J.; Koch, L. *J. Alloys Compd.* **1994**, *213-214*, 456−459.
(41) Garrido, F.; Hannon, A. C.; Ibberson, R. M.; Nowicki, L.; Willis, B. T. M. *Inorg. Chem.* **2006**, *45*, 8408−8413.
(42) Shannon, R. D.; Prewitt, C. T. *Acta Crystallogr., Sect. B* **1969**, *25*, 925−946.
(43) Martin, P. M. Arab-Chapelet, B. Grandjean, S. Arpigny, S.; Welcomme, E. *ESRF experimental form* 2009.
(44) Fujino, T.; Yamashita, T.; Ohuchi, K.; Naito, K.; Tsuji, T. *J. Nucl. Mater.* **1993**, *202*, 154−162.
(45) Thiriet, C.; Konings, R. J. M. *J. Nucl. Mater.* **2003**, *320*, 292−298.
(46) Durazzo, M.; Oliveira, F. B. V.; Urano de Carvalho, E. F.; Riella, H. G. *J. Nucl. Mater.* **2010**, *400*, 183−188.
(47) Kim, J.-G.; Ha, Y.-K.; Park, S.-D.; Jee, K.-Y.; Kim, W.-H. *J. Nucl. Mater.* **2001**, *297*, 327−331.
(48) Kim, H. S.; Yoon, Y. K.; Lee, Y. W. *J. Nucl. Mater.* **1995**, *226*, 206−215.
(49) Ohmichi, T.; Fukushima, S.; Maeda, A.; Watanabe, H. *J. Nucl. Mater.* **1981**, *102*, 40−46.
(50) Kato, M.; Konashi, K. *J. Nucl. Mater.* **2009**, *385*, 117−121.
(51) Nakamura, A.; Masaki, N.; Otobe, H.; Hinatsu, Y.; Wang, J.; Takeda, M. *Pure Appl. Chem.* **2007**, *79*, 1691−1729.
(52) Jankowiak, A.; Maillard, C.; Donnet, L. *J. Nucl. Mater.* **2009**, *393*, 87−91.
(53) Clinard, F. W. Jr.; Hobbs, L. W.; Land, C. C.; Peterson, D. E.; Rohr, D. L.; Roof, R. B. *J. Nucl. Mater.* **1982**, *105*, 248−256.
(54) Ewing, R. C.; Weber, W. J.; Clinard, F. W. *Prog. Nucl. Energy* **1995**, *29*, 63−127.
(55) Kato, M.; Komeno, A.; Uno, H.; Sugata, H.; Nakae, N.; Konashi, K.; Kashimura, M. *J. Nucl. Mater.* **2009**, *393*, 134−140.
(56) Hurtgen, C.; Fuger, J. *Inorg. Nucl. Chem. Lett.* **1977**, *13*, 179−188.
(57) Prieur, D.; Jankowiak, A.; Roudil, D.; Dubois, S.; Leorier, C.; Herlet, N.; Dehaudt, P.; Laval, J.-P.; Blanchart, P. *J. Nucl. Mater.* **2011**, *411*, 15−19.
(58) Prieur, D.; Jankowiak, A.; Leorier, C.; Herlet, N.; Donnet, L.; Dehaudt, P.; Lechelle, J.; Laval, J.-P.; Blanchart, P. *Adv. Sci. Technol.* **2010**, *73*, 104−108.